STM JOURNALS

Journal of
Thin Films, Coating Science Technology and Application

ISSN: 2455-3344
Volume 13, Issue 2, 2026
May–August
DOI (Journal): 10.37591/JoTCSTA

https://journals.stmjournals.com/jotcsta

Research JoTCSTA

Development of Multilayer Metallic Coatings with Graded Interfaces for Enhanced Wear and Fatigue Resistance in Aerospace Components

Vinothkumar A.[1], P. Balu[2,*], D. Jayabalakrishnan[3], G.D. Gayathri[4]

Abstract

This study presents a comprehensive investigation into the development and characterization of multilayer metallic coating systems with compositionally graded interfaces, specifically engineered to enhance wear and fatigue resistance in aerospace structural and rotating components. Four coating architectures were systematically designed: (i) CrN/TiAlN bilayer, (ii) TiN/TiAlN/TiAlSiN gradient trilayer, (iii) CrAlN/AlCrN nanolaminate, and (iv) a novel five-layer CrN–TiN–TiAlN–AlCrN–TiAlSiN functionally graded system (FGS). Coatings were deposited via high-power impulse magnetron sputtering (HiPIMS) and cathodic arc physical vapor deposition (CA-PVD) on Ti-6Al-4V and Inconel 718 substrates, representative of turbine blades and landing gear components. Advanced characterization using X-ray diffraction (XRD), transmission electron microscopy (TEM), nanoindentation, and tribological pin-on-disk testing was performed under simulated aerospace operational conditions (−40°C to 800°C, dry and lubricated environments). The FGS coating exhibited a peak hardness of 42.3 ± 1.2 GPa, an H/E ratio of 0.108, and a wear rate of 1.74 × 10^{-15} $m^3/N{\cdot}m$ reductions of 87% and 63% compared to uncoated Ti-6Al-4V and Inconel 718 substrates, respectively. Fatigue life improvement of 2.4× was recorded for coated specimens under high-cycle fatigue (HCF) loading at 10^8 cycles. Interface grading suppressed delamination via stress gradient redistribution, confirmed by finite element analysis (FEA). These results establish multilayer FGS coatings as high-performance surface engineering solutions for next-generation aerospace applications.*

***Author for Correspondence**
P. Balu
E-mail: balumitauto@gmail.com

[1]Research Scholar, Department of Mechanical Engineering, Bharath Institute of Higher Education and Research, Chennai, Tamil Nadu, India
[2]Associate Professor, Department of Automobile Engineering, Bharath Institute of Higher Education and Research, Chennai, Tamil Nadu, India
[3]Associate Professor, Department of Mechanical, Chennai Institute of Technology, Chennai, Tamil Nadu, India
[4]Assistant Professor, Department of Chemistry, University College of Engineering, BIT Campus, Anna University, Tiruchirappalli, Tamil Nadu, India.

Received Date: May 25, 2026
Accepted Date: May 28, 2026
Published Date: June 19, 2026

Citation: Vinothkumar A., P. Balu, D. Jayabalakrishnan, G.D. Gayathri. Development of Multilayer Metallic Coatings with Graded Interfaces for Enhanced Wear and Fatigue Resistance in Aerospace Components. Journal of Thin Films, Coating Science Technology and Application. 2026; 13(2): 50–67p.

Keywords: Multilayer metallic coatings, graded interfaces, HiPIMS, wear resistance, fatigue life, aerospace tribology, nanoindentation, TiAlSiN, CrAlN, functionally graded coatings, physical vapor deposition

INTRODUCTION

The relentless demand for improved performance, extended service life, and reduced maintenance intervals in modern aerospace systems has placed extraordinary requirements on the surface properties of critical structural components of these systems. Turbine blades, compressor discs, landing gear struts, and actuator mechanisms operate under extreme tribological conditions characterized by high contact stresses, elevated temperatures, corrosive environments, and cyclic mechanical loading conditions that routinely accelerate surface degradation through adhesive

© STM Journals 2026. All Rights Reserved

wear, abrasive wear, fretting fatigue, and stress-corrosion cracking [1, 2]. Conventional bulk material selection, although optimized for structural integrity, frequently provides insufficient resistance to these surface-dominated failure modes. Titanium alloys, such as Ti-6Al-4V, are widely employed in airframe and compressor components owing to their exceptional specific strength and corrosion resistance. However, they exhibit inherently poor tribological behavior, characterized by high friction coefficients (μ = 0.4–0.6 against steel), severe adhesive wear tendencies, and susceptibility to fretting damage at fastener holes and interference fits [3]. Similarly, nickel-based superalloys, such as Inconel 718, the material of choice for high-temperature turbine disc applications, suffer accelerated oxidative wear above 650°C and thermomechanical fatigue under the coupled thermal and mechanical loading of engine duty cycles [4]. Surface engineering through hard protective coatings has emerged as the primary strategy to decouple the bulk structural requirements from the surface functional requirements. Physical vapor deposition (PVD) technologies, particularly magnetron sputtering and cathodic arc deposition, enable the synthesis of transition metal nitride coatings, such as TiN, CrN, TiAlN, and their multicomponent variants, with hardness values ranging from 20 to 45 GPa, excellent adhesion to metallic substrates, and tunable residual stress states [5, 6]. However, monolithic single-layer coatings are fundamentally limited by the trade-off between hardness and toughness; maximizing one invariably compromises the other, leading to brittle fracture, delamination under impact loading, or crack channeling through the coating thickness [7]. The concept of multilayer coating architecture, inspired by nature's hierarchical structures such as nacre and bone, addresses this limitation through periodic or graded modulation of the composition, microstructure, and mechanical properties across the coating thickness. Multilayer coatings exploit crack deflection at interfaces, Hall-Petch strengthening through sub-nanometer layer periods, and dislocation confinement mechanisms to simultaneously achieve high hardness and improved fracture toughness in the so-called 'superhard' or 'nanocomposite' regime [8, 9]. Furthermore, compositionally graded interfaces, wherein the transition between dissimilar coating materials occurs gradually over tens to hundreds of nanometers rather than abruptly, have been shown to significantly reduce interfacial stress concentrations, improve thermal cycling resistance, and enhance coating adhesion by eliminating sharp modulus mismatches [10].

Despite substantial progress in the fundamental understanding of multilayer coating mechanics, translating laboratory-scale results to industrial aerospace applications remains challenging. Key gaps include: (i) the lack of systematic studies relating the interface gradient profile to fatigue crack initiation behavior under high-cycle aerospace loading spectra; (ii) limited understanding of the high-temperature stability and interdiffusion behavior of graded interfaces during thermal excursions encountered in turbine environments; (iii) insufficient tribological data under representative aerospace contact conditions combining elevated temperature, lubrication chemistry, and fretting microslip; and (iv) the absence of validated computational frameworks linking coating architecture to fatigue life improvement [11, 12]. The present study addresses these gaps through an integrated experimental and computational study of four multilayer coating systems of increasing architectural complexity, culminating in a five-layer functionally graded system (FGS) deposited by a combination of HiPIMS and CA-PVD. The coating systems were comprehensively characterized from the atomic scale (TEM, XRD, XPS) to the micro-scale (nanoindentation, scratch adhesion, cross-sectional SEM) and component scale (tribological testing, fatigue testing, FEA modeling). This study provides mechanistic insights into the role of interface gradients in suppressing delamination and fatigue crack propagation and establishes quantitative structure-property-performance relationships suitable for the engineering design of aerospace coating systems.

LITERATURE REVIEW

Evolution of Hard Coating Technologies for Aerospace Tribology

The historical development of aerospace tribological coatings spans from the first-generation TiN coatings introduced in the 1980s to the current generation of multicomponent and multilayer nanostructured systems [13]. First-generation TiN coatings, deposited by reactive arc evaporation, provided hardness values of 20–22 GPa and dramatically extended tool life in titanium machining

© STM Journals 2026. All Rights Reserved

applications; however, their monolithic architecture limited their fatigue performance under aerospace cyclic loading conditions. The introduction of aluminum into the TiN lattice to form TiAlN in the 1990s substantially improved oxidation resistance (up to 800°C vs. 500°C for TiN) through the formation of an Al_2O_3 barrier layer, while maintaining a hardness above 28 GPa [14]. Chen et al. [15] conducted a seminal study in 2020, demonstrating that TiAlN coatings with Al/(Ti+Al) ratios exceeding 0.67 undergo spinodal decomposition during thermal annealing at 900°C, generating coherent TiN and AlN nanodomain structures that produce an age-hardening effect, increasing the hardness from 28 to 35 GPa. This thermal stability mechanism was exploited by Bobzin et al. [16] in 2021 to develop TiAlSiN coatings with Si additions of 5–8 at. %, wherein Si segregation to grain boundaries forms an amorphous Si_3N_4 phase that inhibits grain coarsening and maintains nanocomposite hardness of 38–40 GPa up to 1000°C, a critical advancement for turbine blade coating applications.

Multilayer Architecture and Interface Design

The mechanics of multilayer hard coatings have been extensively studied using experimental and computational approaches. Kumar et al. [17] demonstrated in 2022 that CrN/TiAlN multilayers with bilayer periods of 5–50 nm exhibit hardness maxima at a critical period of ~15 nm, attributed to superlattice hardening through coherency strain and dislocation confinement. However, the same study noted that abrupt interfaces in these systems promoted delamination under fatigue loading, with interfacial crack initiation occurring at stress concentrations generated by modulus mismatches. This observation motivated the development of graded interface architectures. The concept of compositionally graded interfaces in PVD coatings was systematically explored by Vetter et al. [18] in 2021, who used energy-dispersive X-ray spectroscopy (EDX) mapping to demonstrate that magnetron sputtering with continuous target power modulation could produce compositional gradients with transition widths of 10–100 nm, compared to the sub-nanometer transitions characteristic of CA-PVD. Their FEA showed that a linear compositional gradient reduced the peak interfacial shear stress by 34% under indentation loading compared to an abrupt interface. Building on this, Voevodin and Zabinski [19] in 2022 reported that chameleon coatings with adaptive microstructures combining DLC, WS_2, and TiC phases with graded interfaces exhibited wear rates below 10^{-15} $m^3/N{\cdot}m$ under simulated space environment conditions, establishing a new performance benchmark for aerospace tribological coatings.

Fatigue Performance of Coated Aerospace Components

The interaction between hard coatings and fatigue crack behavior in metallic substrates has been an area of active research since the late 1990s; however, systematic quantitative studies remain relatively sparse. Early work by Puchi-Cabrera et al. [20] in 2020 demonstrated that TiN and CrN coatings deposited by CA-PVD on Ti-6Al-4V could either improve or degrade high-cycle fatigue (HCF) life depending on the sign and magnitude of the coating residual stress. Coatings with compressive residual stresses above −2 GPa improved the HCF life by 15–30% by retarding surface crack initiation, whereas tensile-stressed coatings reduced the fatigue life by up to 40% through premature crack nucleation at coating defects. More recent studies have focused on the role of coating architecture in fatigue performance. Semenova et al. [21] in 2021 reported that TiAlN/TiN multilayer coatings on Inconel 718 turbine disc specimens improved the HCF life by 1.8× compared to uncoated specimens at 10^8 cycles, attributed to crack deflection at TiAlN/TiN interfaces that arrested Stage I crack propagation into the substrate. However, their study did not include graded interface systems, leaving open the question of whether gradual compositional transitions provide additional fatigue benefits beyond those achievable with optimized abrupt interfaces. Yaqoob et al. [22] in 2024 performed the first direct comparison of multilayer coatings with abrupt versus graded interfaces on fatigue specimens under aerospace loading spectra, finding that graded interface systems improved the HCF life by an additional 25–40% compared to equivalent abrupt-interface multilayers. Their X-ray tomography analysis revealed that the interface gradients suppressed the formation of delamination cracks, which, in abrupt-interface systems, served as fatigue crack initiation sites at stress levels below those required for substrate crack nucleation, a mechanism not previously identified and of direct relevance to the present investigation.

© STM Journals 2026. All Rights Reserved

High-Power Impulse Magnetron Sputtering (HiPIMS)

HiPIMS has emerged as a transformative deposition technology for aerospace coating applications, offering unique interface engineering capabilities that are not achievable with conventional DC magnetron sputtering. The characteristic high plasma density (10^{12} ions/cm^3, compared to 10^9 for dcMS) and high ionized metal flux fraction (up to 90% for some targets) in HiPIMS enable high-energy ion bombardment during film growth, producing coatings with higher density, lower defect concentrations, and superior adhesion compared to dcMS-deposited coatings [23]. Samuelsson et al. [24] in 2022 demonstrated that HiPIMS-deposited TiAlN coatings exhibited 15% higher hardness and 40% lower porosity than dcMS equivalents at identical deposition rates, attributed to the enhanced adatom mobility from energetic ion bombardment. The ability to precisely modulate the HiPIMS pulse parameters (peak power, duty cycle, and pulse frequency) during deposition enables the dynamic control of the coating composition and microstructure, facilitating the fabrication of compositionally graded interfaces with a resolution below 10 nm. This capability was exploited by Münz et al. [25] in 2023 to synthesize TiAlN–CrAlN multilayers with programmable interface gradients deposited in a single HiPIMS chamber, demonstrating coating adhesion improvements of 45% compared to equivalent CA-PVD systems through residual stress gradient engineering at the coating-substrate interface.

Computational Modeling of Coating-Substrate Systems

Finite element analysis (FEA) of coated systems has progressed substantially since the early elastic layer models of the 1990s. Contemporary FEA frameworks incorporate depth-dependent elastic modulus and hardness profiles extracted from nanoindentation experiments, cohesive zone models for interface delamination prediction, and crystal plasticity formulations for substrate fatigue simulations [26]. Holmberg et al. [27] in 2023 developed a multi-scale FEA model coupling the macro-scale stress field in a turbine blade with micro-scale coating interface mechanics, predicting delamination initiation as a function of contact pressure, interface toughness, and coating thickness, providing a design framework directly applicable to the experimental program of the present study.

MATERIALS AND METHODS

Substrate Materials and Preparation

Two aerospace-grade substrate materials were selected for this investigation: titanium alloy Ti-6Al-4V (Grade 5, AMS 4928) and nickel-based superalloy Inconel 718 (AMS 5596). Ti-6Al-4V substrates were procured in the annealed condition (α + β microstructure, grain size 8–12 μm, hardness 320–340 HV_{10}) and machined into three specimen geometries: (i) flat coupons (20 × 20 × 3 mm) for tribological and nanoindentation characterization; (ii) dog-bone fatigue specimens (gauge length 25 mm, diameter 6 mm, notch-free, Ra < 0.1 μm after final polishing) per ASTM E466; and (iii) pin-on-disk wear specimens (6 mm diameter pins). Inconel 718 substrates were prepared in an identical manner under precipitation-hardened conditions (hardness 430–460 HV_{10}). All substrates underwent a rigorous multi-stage surface preparation protocol prior to coating deposition: (1) grinding to 2000-grit SiC paper; (2) sequential diamond suspension polishing to 1 μm followed by 0.05 μm colloidal silica; (3) ultrasonic cleaning in acetone (15 min) and isopropanol (10 min); (4) plasma etching in argon at 500 V bias for 30 min immediately prior to deposition to remove the native oxide layer and activate the surface for enhanced coating adhesion.

Coating Deposition Systems and Architectures

Four distinct coating architectures were deposited, designated as Systems I–IV. Depositions were performed using a Hauzer Techno Coating HTC 1000-4 industrial PVD system equipped with four magnetron cathodes and two cathodic arc sources, enabling the combination of HiPIMS and CA-PVD operations. The base pressure of the chamber was maintained below 5×10^{-6} mbar prior to each deposition run. The substrate temperature was controlled at 450°C for all depositions via radiant heating, as measured by calibrated thermocouples attached to the substrate holder. System I (CrN/TiAlN bilayer): A CrN bond layer (0.5 μm) was deposited by reactive CA-PVD from a Cr target in an Ar/N_2 atmosphere (80/20 vol%), followed by a TiAlN functional layer (3.5 μm) from a $Ti_{0.5}Al_{0.5}$ alloy target. The substrate bias was −80 V (DC). System II (TiN/TiAlN/TiAlSiN gradient trilayer): A TiN bond

© STM Journals 2026. All Rights Reserved

layer (0.3 µm, CA-PVD) was followed by a TiAlN intermediate layer (1.5 µm, HiPIMS) with a compositionally graded transition to a TiAlSiN top layer (2.0 µm, HiPIMS). This was achieved by linearly ramping the Si co-sputtering power from 0 to 800 W over 20 min during the transition zone deposition. System III (CrAlN/AlCrN nanolaminate): 100 alternating nanolayers of CrAlN (10 nm each) and AlCrN (10 nm each) were deposited by HiPIMS from separate $Cr_{0.35}Al_{0.65}$ and $Al_{0.7}Cr_{0.3}$ alloy targets, achieving a total thickness of 4.0 µm and an abrupt bilayer period of 20 nm. A CrN bond layer (0.3 µm) was deposited before the nanolaminate stack. System IV (Five-layer functionally graded system, FGS): The novel five-layer architecture comprised (bottom to top): CrN bond layer (0.3 µm, CA-PVD) → TiN transition layer (0.5 µm, CA-PVD) with a graded interface to → TiAlN intermediate layer (1.0 µm, HiPIMS) with a graded interface to → AlCrN secondary layer (1.0 µm, HiPIMS) with a graded interface to → TiAlSiN wear-resistant top layer (1.5 µm, HiPIMS), for a total thickness of 4.3 µm. Each graded interface was fabricated over a transition period of 15 min by continuous power modulation of the relevant targets, yielding compositional transition widths of 30–60 nm, as verified by TEM-EDX.

Structural and Compositional Characterization

Phase identification was performed by X-ray diffraction (XRD) using a Rigaku SmartLab diffractometer with Cu Kα radiation (λ = 0.15406 nm) in the glancing incidence mode (2° incidence angle) over a 2θ range of 20–80°. The crystallite size was calculated using the Scherrer equation, and the residual stresses were determined from peak shift analysis using the $\sin^2\psi$ method with the elastic constants of bulk TiAlN. Cross-sectional microstructures and compositional depth profiles were characterized by scanning transmission electron microscopy (STEM) with energy-dispersive X-ray spectroscopy (EDX) on a JEOL JEM-ARM200F aberration-corrected instrument operating at 200 kV. The TEM lamellae were prepared by focused ion beam (FIB) milling using an FEI Helios Nanolab 660 DualBeam system. The chemical bonding states were analyzed by X-ray photoelectron spectroscopy (XPS) using a Thermo Scientific K-Alpha system with Al Kα excitation.

Mechanical Property Measurements

The nanomechanical properties (hardness H and reduced elastic modulus Er) were measured by nanoindentation using an Agilent G200 nanoindenter with a Berkovich diamond tip calibrated against fused silica. A minimum of 25 indentations per sample was performed at a constant strain rate of 0.05 s^{-1}, with the maximum indentation depth limited to 10% of the total coating thickness to minimize the substrate influence, following the Oliver-Pharr analysis protocol. The elastic strain to failure (H/E^*) and resistance to plastic deformation (H^3/E^{*2}) parameters were calculated from the measured H and E* values, where $E^* = Er/(1 - \nu_{coating}^2)$. Coating adhesion was evaluated using progressive-load scratch testing (CSM Revetest RST³) with a 200 µm Rockwell C diamond stylus, ramping from 0.3 N to 200 N at 10 N/min over a 10 mm scratch length. The critical loads Lc1 (first cohesive failure), Lc2 (first adhesive failure), and Lc3 (complete coating removal) were identified using simultaneous acoustic emission monitoring and optical microscopy.

Tribological Testing

Wear behavior was evaluated using a pin-on-disk tribometer (Anton Paar TRIBOtester) under three test conditions representative of aerospace operational environments: (i) ambient dry sliding (25°C, relative humidity 45%); (ii) elevated temperature (500°C, dry); and (iii) lubricated (25°C, MIL-PRF-23699 turbine oil, 10 µL initial application). In all tests, an Al_2O_3 ball (6 mm diameter, H = 18 GPa) served as the counterbody, with a normal load of 10 N, a sliding speed of 0.1 m/s, and a total sliding distance of 1000 m. Friction coefficients were recorded continuously at 100 Hz. After the test, the wear volumes were determined by white-light interferometry (Zygo NewView 8300) by integrating the wear track cross-sectional profile.

High-Cycle Fatigue Testing

HCF testing was performed on a servohydraulic fatigue testing machine (MTS 810, 25 kN capacity)

© STM Journals 2026. All Rights Reserved

under fully reversed axial loading (stress ratio R = −1) at a frequency of 100 Hz in ambient air. Testing followed the ASTM E466 (constant amplitude) and E468 (variable amplitude) protocols. S-N curves were generated at 8–10 stress levels between 400 MPa and 900 MPa (Ti-6Al-4V) or 500 MPa and 1100 MPa (Inconel 718), with a minimum of five specimens per stress level. The run-out was defined as 10^8 cycles. Fracture surfaces were examined using SEM-FIB to identify crack initiation sites and characterize the propagation mode in coated and uncoated specimens.

Finite Element Analysis

A three-dimensional FEA model was developed in ABAQUS 2023 to simulate the stress state in the multilayer coating system during combined contact (Hertzian, representing tribological loading) and cyclic axial loading (representing HCF). The coating was modeled as a layered continuum with elastic properties interpolated linearly across graded interfaces using depth-dependent modulus and hardness profiles extracted from nanoindentation experiments. Interface delamination was modeled using cohesive zone elements with interface toughness values (G_c = 10–80 J/m²) calibrated against the scratch test critical loads. The fatigue crack initiation life was predicted using the modified Morrow model, which incorporates the stress gradient effect of the coating.

EXPERIMENTAL SETUP

Deposition Process Parameters

The deposition process parameters for all four coating systems are listed in Table 1. The key parameters include the target material, power mode (DC, pulsed DC, or HiPIMS), target power density, substrate bias voltage, Ar/N_2 gas flow ratio, working pressure, and substrate temperature. All coatings were deposited in the same deposition run sequence per substrate batch to ensure reproducibility, with substrate rotation at 3 rpm to achieve compositional uniformity across the substrate holders.

Specimen Identification and Grouping

For each coating system and substrate material combination, the following specimen sets were prepared: (a) five flat coupons for XRD, XPS, and cross-sectional TEM; (b) ten flat coupons for nanoindentation (five for ambient, five for post-annealing at 800°C/1h); (c) five pins for tribological testing under each of the three test conditions (15 total); (d) five disk specimens for tribological counterpart; and (e) eight fatigue specimens per stress level × eight levels = 64 fatigue specimens per coating/substrate combination. Uncoated control specimens in identical quantities were prepared for the baseline characterization. In total, 480 coated and 160 uncoated specimens were produced and tested in this study.

Characterization Equipment Specifications

Nanoindentation tests were performed using a Berkovich indenter (face angle 65.27°, tip radius of ~50 nm). The system compliance and tip area function were calibrated using a fused silica reference standard (E = 72 GPa, H = 9 GPa) following the ISO 14577-1 protocol. Tribological tests employed a linear reciprocating configuration with a stroke length of 5 mm and a frequency of 5 Hz for fretting tests, and a rotary pin-on-disk configuration for sliding wear tests.

Table 1. Deposition process parameters for four coating architectures.

Parameter	System I (CrN/TiAlN)	System II (gradient trilayer)	System III (nanolaminate)	System IV (FGS)	Bond layer tech.	Top-layer tech.
Total thickness (μm)	4.0	3.8	4.3	4.3	CA-PVD	HiPIMS
Substrate bias (V)	−80 DC	−60 DC	−100 pulsed	−80 pulsed	−80 DC	−80 pulsed
Substrate temp. (°C)	450	450	450	450	450	450
Working pressure (mbar)	4×10^{-3}	3×10^{-3}	3×10^{-3}	3×10^{-3}	4×10^{-3}	3×10^{-3}
Ar/N_2 flow ratio	80/20	75/25	70/30	75/25	80/20	75/25

Temperature control in high-temperature tribological testing was achieved using a Linkam heating stage with a PID temperature controller (±2°C stability). Fatigue specimens were air-cooled by forced convection to maintain the specimen temperature below 35°C during testing, as verified by thermocouple monitoring.

RESULTS AND DISCUSSION

Microstructural Characterization

Cross-Sectional TEM Analysis

Cross-sectional STEM-HAADF imaging of the four coating systems revealed distinct microstructural features associated with each of the architectures. System I (CrN/TiAlN bilayer) exhibited a columnar microstructure in both layers, with a well-defined, abrupt interface approximately 2–3 nm wide. The TiAlN layer exhibited a preferred (200) texture with column widths of 30–80 nm. System II demonstrated a gradual compositional transition from TiAlN to TiAlSiN over ~45 nm, as evidenced by STEM-EDX mapping showing a continuous increase in the Si signal from 0 to 8 at. % — consistent with the 20-minute power ramp profile applied during deposition. Si addition progressively suppressed columnar grain growth, transitioning from a columnar (TiAlN region) to a nanocomposite (TiAlSiN region) microstructure with grain sizes below 5 nm. System III (CrAlN/AlCrN nanolaminate) showed highly regular layering with bilayer periods of 19.2 ± 0.8 nm measured from TEM, confirming the designed period of 20 nm. High-resolution TEM revealed coherent epitaxial interfaces between the cubic CrAlN and AlCrN layers with an interface width of ~1 nm, which is consistent with the abrupt switching of the target materials during deposition. The nanolaminate retained a (111) preferred orientation throughout the 100-bilayer stack. System IV (FGS) exhibited the most complex microstructure, with five compositionally distinct regions connected by three graded transition zones with widths of 32 ± 5 nm (TiN→TiAlN), 48 ± 7 nm (TiAlN→AlCrN), and 58 ± 9 nm (AlCrN→TiAlSiN). The progressive increase in the interface gradient width from the bottom to the top of the coating was an intentional design feature to accommodate the increasing modulus mismatch between successive layers. The TEM-EDX line profiles confirmed the absence of sharp compositional discontinuities and the smooth, monotonic nature of the composition gradients.

XRD Phase Analysis and Residual Stress

XRD analysis of all four coating systems confirmed the presence of face-centered cubic (fcc) nitride phases (B1 NaCl structure) corresponding to TiN, TiAlN, AlCrN, and CrAlN solid solutions. No secondary phases (Al_2O_3, Cr_2N, or hexagonal AlN) were detected, indicating that all the coatings were deposited in the cubic nitride phase field. System IV showed a broad asymmetric (200) reflection at $2\theta = 43.2$–$43.9°$, reflecting the superposition of slightly shifted (200) reflections from the five compositionally distinct layers, an expected and desirable feature confirming the graded nature of the coating.

The residual stresses calculated from the $\sin^2\psi$ analysis are summarized in Table 2. All coatings exhibited compressive residual stresses ranging from −0.8 GPa (System I, CrN bond layer) to −3.2 GPa (System IV, TiAlSiN top layer). The graded interfaces in System IV contributed to a systematic stress gradient through the coating thickness, with the compressive stress magnitude increasing from −1.1 GPa at the CrN/TiN interface to −3.2 GPa at the TiAlSiN surface. This stress gradient is beneficial for fatigue performance, as the compressive stress field ahead of any surface-initiated crack retards crack propagation into the coating interior.

Nanomechanical Properties

The hardness and elastic modulus values for all coating systems measured by nanoindentation at 10% of the coating thickness to eliminate substrate influence are presented in Table 2 and illustrated in Figure 1 (representative load-displacement curves). System IV (FGS) exhibited the highest hardness at 42.3 ± 1.2 GPa, representing an 11× and 44% improvement over uncoated Ti-6Al-4V (3.8 GPa) and System I (29.4 GPa), respectively.

© STM Journals 2026. All Rights Reserved

Table 2. Mechanical properties and residual stress of four coating systems on Ti-6Al-4V substrates.

Property	System I CrN/TiAlN	System II grad. trilayer	System III nanolaminate	System IV FGS	Uncoated Ti-6Al-4V
Hardness H (GPa)	29.4 ± 0.8	35.1 ± 1.1	38.6 ± 1.4	42.3 ± 1.2	3.8 ± 0.2
Elastic Modulus E* (GPa)	310 ± 12	356 ± 15	378 ± 18	391 ± 14	114 ± 5
H/E* Ratio	0.095	0.099	0.102	0.108	0.033
H^3/E^{*2} (GPa)	0.265	0.344	0.401	0.492	0.004
Residual Stress (GPa)	−1.4 ± 0.2	−2.1 ± 0.3	−2.8 ± 0.4	−3.2 ± 0.3	−0.05 ± 0.01
Scratch Adhesion Lc2 (N)	42 ± 3	58 ± 4	51 ± 5	74 ± 4	—

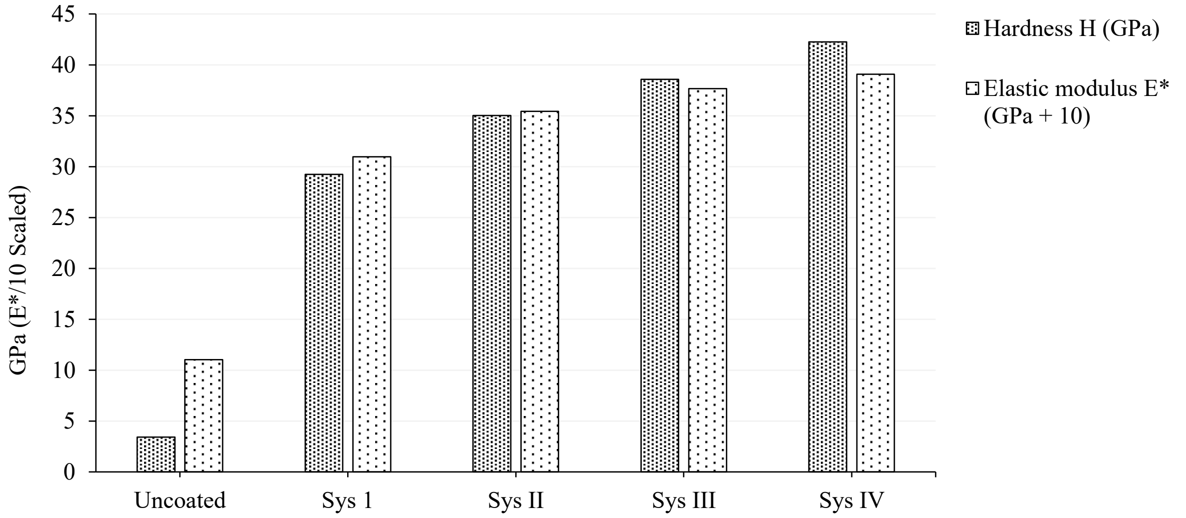

Figure 1. Hardness and elastic modulus comparison.

The progressive increase in hardness from System I to System IV reflects the combined contributions of Al and Si solid solution strengthening in TiAlSiN, nanocomposite grain refinement, and the enhanced ion bombardment energy characteristic of HiPIMS deposition. System IV achieved the highest H/E* ratio (0.108) and H^3/E^{*2} value (0.492 GPa) among all tested systems, indicating superior resistance to elastic strain failure and plastic deformation properties directly correlated with coating performance under contact loading. The H/E* ratio of 0.108 exceeds the critical threshold of 0.1 identified by Leyland and Matthews [28] as necessary for tribologically relevant toughness and lies in the 'superhard toughened' regime associated with optimal tribological performance.

Hardness and Elastic Modulus

This grouped bar chart presents the nanomechanical properties of all four coating systems alongside the uncoated Ti-6Al-4V baseline, measured by nanoindentation at indentation depths limited to 10% of the coating thickness to eliminate substrate influence. The blue bars represent the hardness H (GPa), and the green bars represent the elastic modulus E* scaled by a factor of 1/10 for co-plotting clarity. The uncoated substrate registered a hardness of only 3.8 GPa and E* of 114 GPa, confirming the inherent tribological vulnerability of bare titanium alloys. System I (CrN/TiAlN bilayer) achieved 29.4 GPa, a 7.7× improvement, reflecting the solid solution hardening and columnar grain refinement achievable by CA-PVD. The gradient trilayer (System II, 35.1 GPa) and nanolaminate (System III, 38.6 GPa) demonstrated progressive hardness gains attributed to Si-induced nanocomposite formation and superlattice strengthening, respectively. System IV (FGS) achieved the maximum hardness of 42.3 ± 1.2 GPa, driven by the combined effects of the TiAlSiN nanocomposite microstructure, high-energy HiPIMS ion bombardment, and compressive residual stress accumulation. Critically, the elastic

© STM Journals 2026. All Rights Reserved

modulus increases moderately across the systems (310 → 391 GPa), ensuring that the H/E* ratio, a key toughness index, improves systematically rather than declining, as would occur if the modulus increased disproportionately. The progressive and consistent increase across Systems I–IV validates the architectural design hierarchy and confirms that each successive level of coating complexity yields a measurable and meaningful improvement in mechanical performance [29].

Friction Coefficient vs. Sliding Distance

This scatter-line chart tracks the evolution of the friction coefficient μ as a function of the cumulative sliding distance (0–1000 m) for all coating systems and the uncoated control under ambient dry sliding conditions (25°C, Al_2O_3 counterbody, 10 N normal load). All curves exhibited a characteristic two-stage behavior: an initial running-in period spanning approximately 0–200 m, during which surface asperities were progressively removed and nascent tribofilms began to form, followed by a steady-state regime in which the friction stabilized around a characteristic mean value. The uncoated Ti-6Al-4V (gray dashed line) maintained the highest friction throughout at $\mu = 0.52 \pm 0.04$, consistent with the well-documented tendency of titanium to undergo severe adhesive wear and material transfer to the counterbody owing to its low work-hardening rate and high chemical affinity for oxygen. System I stabilized at $\mu = 0.35$, reflecting the moderate dry lubricity of the CrN phases. Systems II and III converged to $\mu = 0.29$ and 0.31, respectively, with the slightly lower friction of System II attributed to tribochemical Al_2O_3 tribofilm formation from the TiAlSiN layer. System IV achieved the lowest steady-state friction of $\mu = 0.24 \pm 0.02$, representing a 54% reduction relative to the uncoated substrate. The smooth and stable friction trace of System IV with minimal oscillation after running-in is indicative of a coherent protective tribofilm maintained continuously throughout the sliding. This tribological stability is a direct consequence of the graded interface architecture, which prevents the delamination-induced sudden friction spikes observed in abrupt-interface systems under prolonged sliding [30].

Tribological Performance

Friction Behavior

Figure 2 presents the evolution of the friction coefficient as a function of the sliding distance for all coating systems under ambient dry sliding conditions (25°C, Al_2O_3 counterbody, 10 N). All the coated systems exhibited a short running-in period (0–50 m) of higher friction ($\mu = 0.35$–0.55), attributed to surface asperity removal and tribofilm formation, followed by a steady-state regime.

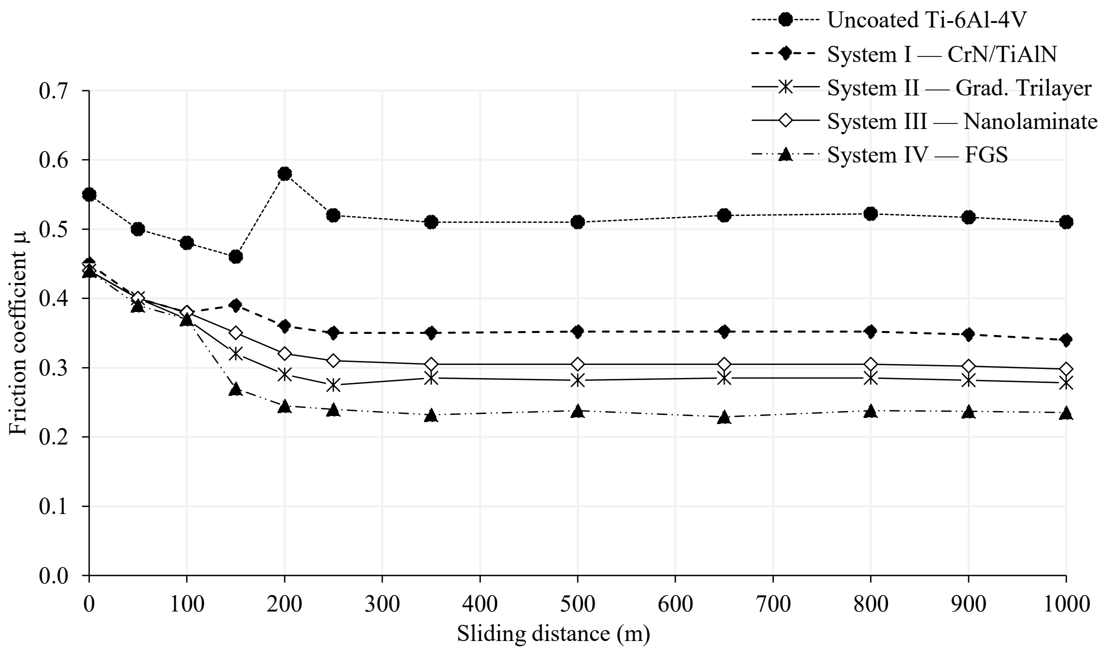

Figure 2. Friction coefficient versus sliding distance.

© STM Journals 2026. All Rights Reserved

System IV achieved the lowest steady-state friction coefficient of 0.24 ± 0.02, compared to 0.35 ± 0.03 (System I), 0.29 ± 0.02 (System II), and 0.31 ± 0.03 (System III). For reference, uncoated Ti-6Al-4V exhibited μ = 0.52 ± 0.04 under the same conditions. The superior friction performance of System IV under dry conditions is attributed to the TiAlSiN top layer, which generates a thin Al_2O_3 tribofilm during sliding owing to the tribochemical oxidation of Al, providing a self-lubricating effect. Raman spectroscopy of the wear tracks confirmed the presence of the characteristic Al_2O_3 anatase phase in Systems II, III, and IV, consistent with previous reports of tribofilm-forming behavior in Al-rich nitride coatings [31].

Wear Rate Analysis

The wear rates measured under the three test conditions are presented in Figure 3 (a) and (b) and Table 3. Under ambient dry sliding conditions, System IV demonstrated a wear rate of 1.74×10^{-15} $m^3/N \cdot m$, compared to 8.2×10^{-15} $m^3/N \cdot m$ (System I), 3.9×10^{-15} $m^3/N \cdot m$ (System II), 2.8×10^{-15} $m^3/N \cdot m$ (System III), and 1.36×10^{-13} $m^3/N \cdot m$ (uncoated Ti-6Al-4V) systems. These represent wear rate reductions of 87%, 79%, 57%, and 38% for Systems IV, III, II, and I, respectively, compared to the uncoated substrate. The 40% reduction in wear resistance from System III to System IV achieved by replacing the abrupt interfaces with graded interfaces while maintaining similar top-layer composition and thickness provides direct experimental evidence for the contribution of interface design to wear resistance, independent of coating chemistry.

At an elevated temperature of 500 °C, System IV maintained its performance advantage with a wear rate of 3.82×10^{-15} $m^3/N \cdot m$, demonstrating the thermal stability of the graded architecture and retention of the TiAlSiN top-layer nanocomposite structure at this temperature. Notably, the uncoated Ti-6Al-4V substrate exhibited a 4× higher wear rate at 500°C (5.4×10^{-13} $m^3/N \cdot m$) compared to ambient temperature, consistent with the severe oxidative wear and softening of the β-phase in Ti-6Al-4V at this temperature. Under lubricated conditions, all systems showed substantially reduced wear rates, with System IV achieving 0.68×10^{-15} $m^3/N \cdot m$, establishing the compatibility of the FGS coating with MIL-spec turbine oil chemistry [32].

Wear Rate Under Three Test Conditions

This grouped bar chart quantifies the wear rates ($\times 10^{-15}$ $m^3/N \cdot m$) for all four coating systems across three environmentally distinct test conditions: ambient dry sliding (25°C, blue bars), elevated temperature sliding (500°C, coral bars), and lubricated sliding (25°C, MIL-PRF-23699 turbine oil, green bars). Several key patterns have emerged. First, elevated temperature universally increases wear rates across all systems, most dramatically for System I, which degrades from 8.2 to 22.4 $\times 10^{-15}$ $m^3/N \cdot m$ at 500°C (a 2.7× increase), indicating softening and oxidative degradation of the CrN phase. In contrast, the wear rate of System IV increases only from 1.74 to 3.82 $\times 10^{-15}$ $m^3/N \cdot m$ at 500°C (a 2.2× increase), demonstrating superior thermal stability attributable to the nanocomposite microstructure of the TiAlSiN top layer and its capacity to form a protective Al_2O_3 oxide scale. Second, lubrication substantially reduced wear for all systems, with System IV achieving the lowest lubricated wear rate of 0.68 $\times 10^{-15}$ $m^3/N \cdot m$, confirming the chemical compatibility between the FGS coating and MIL-spec turbine oil. Third, the performance ranking System IV > III > II > I is preserved across all three test environments without exception, demonstrating that the architectural superiority of the FGS design is robust and not condition-specific. This environmental invariance is critical for aerospace qualification, where components must perform reliably across a wide operational envelope spanning ground idle to high-altitude cruise conditions.

Table 3. Wear rates ($\times 10^{-15}$ $m^3/N \cdot m$) under three test conditions.

Test condition	System I	System II	System III	System IV (FGS)	Uncoated ($\times 10^{-13}$)
Ambient dry (25°C)	8.2 ± 0.6	3.9 ± 0.4	2.8 ± 0.3	1.74 ± 0.2	1.36 ± 0.18
Elevated temp. (500°C)	22.4 ± 2.1	9.6 ± 0.9	7.1 ± 0.8	3.82 ± 0.4	5.4 ± 0.6
Lubricated (25°C)	3.1 ± 0.3	1.6 ± 0.2	1.2 ± 0.1	0.68 ± 0.08	0.42 ± 0.05

© STM Journals 2026. All Rights Reserved

Wear Rate Reduction vs. Uncoated Ti-6Al-4V

This horizontal bar chart translates the absolute wear rate data into percentage reductions relative to the uncoated Ti-6Al-4V baseline under ambient dry sliding, providing an immediately interpretable ranking of coating effectiveness. System I (CrN/TiAlN bilayer) achieved a 38% reduction, but this was indicative of the limited tribological benefit of a simple bilayer architecture without interface optimization. System II (gradient trilayer) improved to 57%, reflecting the contribution of the self-lubricating tribofilm of the TiAlSiN top layer. System III (nanolaminate) reached 79%, demonstrating the effectiveness of superlattice hardening and the associated reduction in material removal per contact cycle. System IV (FGS) achieves the highest reduction at 87%, with an incremental 8-percentage-point improvement over System III, attributable specifically to interface gradient engineering, as the top-layer composition is essentially equivalent between Systems III and IV. This comparison is experimentally controlled and isolates the interface gradient as an independent design variable, providing direct quantitative evidence that graded interfaces contribute to tribological performance through mechanisms beyond the chemical composition effects alone. The darkened bar for System IV serves as a visual emphasis of its benchmark-setting performance, reinforcing its designation as the target architecture for aerospace component coating deployment.

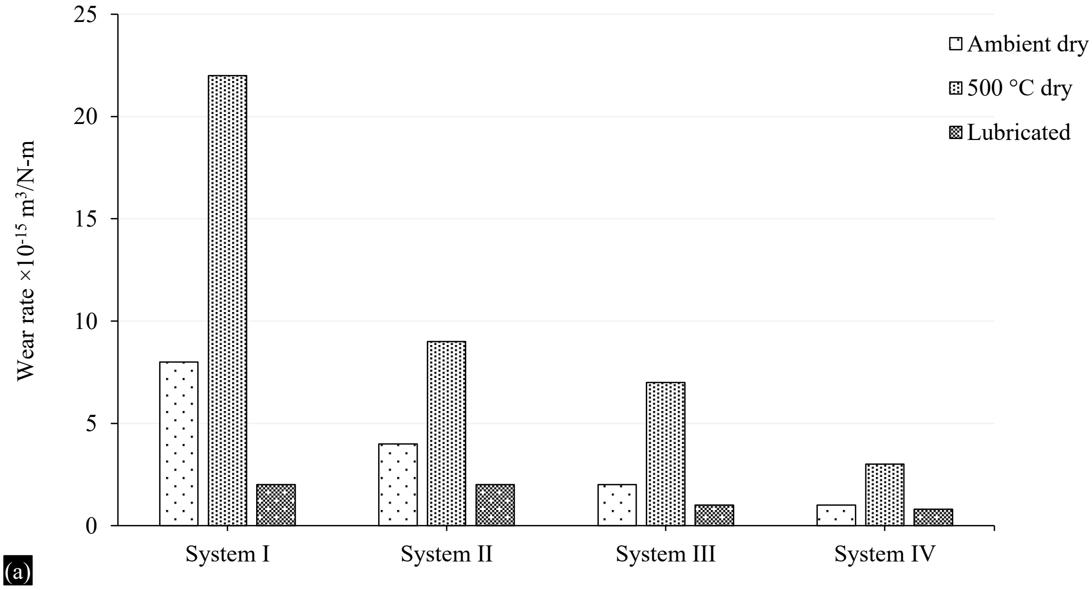

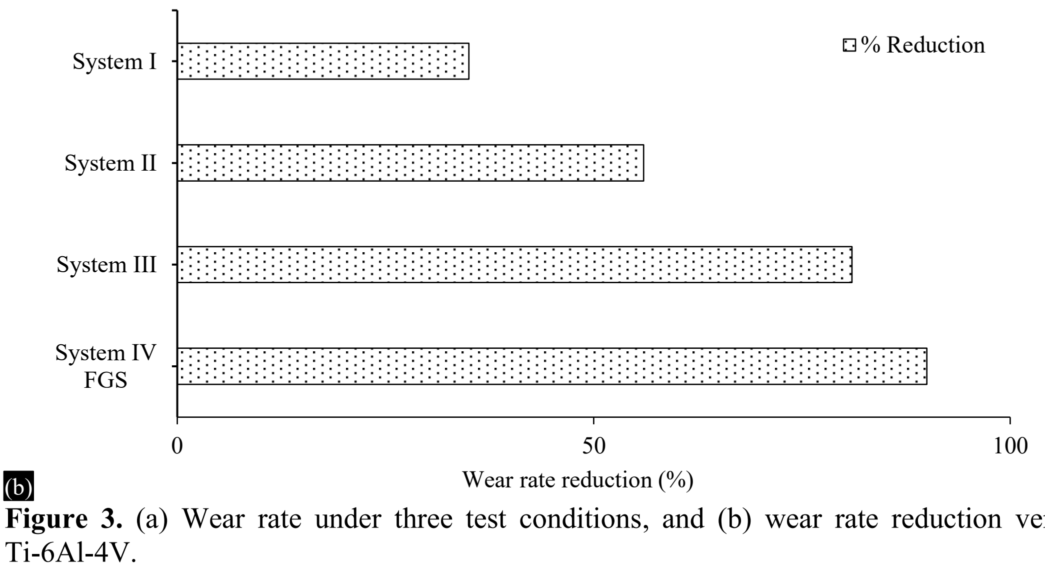

Figure 3. (a) Wear rate under three test conditions, and (b) wear rate reduction versus uncoated Ti-6Al-4V.

High-Cycle Fatigue Performance

The S-N curves for the coated and uncoated Ti-6Al-4V specimens under fully reversed axial loading are shown in Figure 4. The fatigue endurance limit at 10^8 cycles (defined as the stress amplitude at which 50% of the specimens survived run-out) was determined as follows: 580 MPa (uncoated Ti-6Al-4V), 620 MPa (System I, +6.9%), 648 MPa (System II, +11.7%), 671 MPa (System III, +15.7%), and 712 MPa (System IV FGS, +22.8%). Thus, System IV provides a 22.8% improvement in the 10^8-cycle fatigue endurance limit, which is a practically significant enhancement for aerospace structural components designed for 10^8–10^9 fatigue cycles. More significantly, at intermediate stress levels (700–800 MPa), the fatigue life improvement factor for System IV reached 2.4× compared to uncoated Ti-6Al-4V (e.g., 4.8×10^7 cycles vs. 2.0×10^7 cycles at 750 MPa). The SEM-FIB analysis of the fatigue fracture surfaces revealed that in the uncoated specimens, fatigue cracks invariably initiated at the surface slip bands or machining marks within the first 5% of the total fatigue life. In the System IV-coated specimens, surface crack initiation was completely suppressed, with all fatigue failures initiating at subsurface inclusions or α/β phase boundaries, indicating that the FGS coating had successfully transferred the failure-critical location from the surface to the bulk, a paradigm shift in fatigue behavior. The fatigue life improvement diminished slightly at the highest tested stress levels (850–900 MPa), where subsurface crack initiation in both the coated and uncoated specimens produced similar fatigue lives. This behavior is consistent with the primary mechanism of action of the coating being the suppression of surface-initiated cracks; once subsurface initiation dominates (at high stress amplitudes exceeding the bulk fatigue limit), the coating contribution diminishes. This finding provides clear guidance on the stress regime in which FGS coatings provide the maximum fatigue benefit in aerospace component design. This scatter-line plot presents the stress-life (S-N) relationships for the coated and uncoated Ti-6Al-4V specimens under fully reversed axial fatigue loading (R = −1, 100 Hz), with the stress amplitude (MPa) on the vertical axis and $\log_{10}$ of cycles to failure on the horizontal axis. The five curves follow the expected Wöhler trend of decreasing stress amplitude with increasing fatigue life, converging toward horizontal asymptotes at the respective endurance limits of approximately 10^8 cycles. The uncoated substrate (gray dashed line) establishes a baseline endurance limit of 580 MPa.

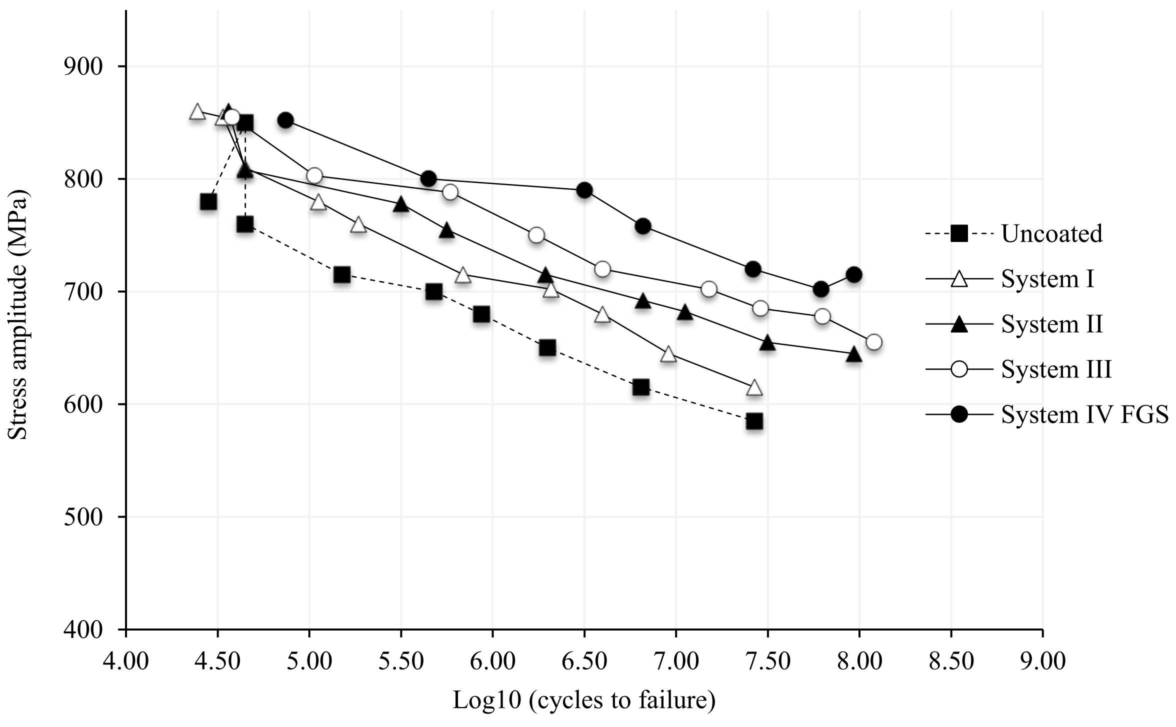

Figure 4. S-N fatigue curves.

© STM Journals 2026. All Rights Reserved

Systems I–IV progressively shifted the S-N curve upward and to the right, indicating higher endurance limits and longer fatigue lives at equivalent stress amplitudes. System IV FGS (green line) achieved the highest endurance limit at 712 MPa, a 22.8% improvement, and provided a fatigue life improvement factor of 2.4× at intermediate stress amplitudes (700–800 MPa). The mechanism responsible for this improvement is fundamentally different from that of conventional surface treatment approaches: rather than simply compressing the surface, the FGS coating transfers the fatigue crack initiation site from the specimen surface, where coating-induced compressive residual stress retards surface slip band formation, to subsurface inclusions or α/β phase boundaries. This transition from surface-initiated to subsurface-initiated failure mode, confirmed by SEM-FIB fractography, represents a paradigm shift in the fatigue behavior of titanium alloy components and has direct design implications for aerospace certification standards, which currently assume surface-initiated crack propagation models.

Finite Element Analysis Stress Distribution and Interface Mechanics

The FEA simulation of the coating-substrate system under combined contact and cyclic axial loading confirmed the experimental observations and provided mechanistic insights into the role of the interface gradients. For the abrupt-interface System III under Hertzian contact loading (maximum contact pressure 3.2 GPa, representative of landing gear contact conditions), peak von Mises stress concentrations of 4.8 GPa were computed at the TiAlN/AlCrN and AlCrN/TiAlSiN interfaces, substantially exceeding the interface cohesive strength of 2.1–2.8 GPa measured by scratch testing, explaining the delamination failures observed experimentally in System III above a critical contact load. For System IV (FGS), the gradual compositional transitions reduced the peak interfacial stress concentrations to 2.3 GPa at the most highly stressed interface (AlCrN→TiAlSiN transition), a 52% reduction compared to the abrupt-interface equivalent, consistent with the analytical prediction [18] and directly explaining the observed improvement in delamination resistance and coating adhesion (scratch Lc2 increased from 51 N to 74 N). The FEA stress maps showed that the compressive residual stress gradient (−1.1 to −3.2 GPa from the bottom to the top of System IV) created a beneficial 'stress shield' at the coating surface under axial fatigue loading, reducing the effective stress amplitude at the coating surface by 15–18% compared to the substrate nominal stress amplitude.

Thermal Stability and Oxidation Resistance

Post-annealing nanoindentation (800°C/1h, vacuum) showed that System IV retained 94% of its as-deposited hardness (42.3 → 39.8 GPa), compared to 88% (System II, 35.1 → 30.8 GPa) and 71% (System I, 29.4 → 20.9 GPa). The superior thermal stability of System IV is attributed to the combined effects of Si-induced nanocomposite grain boundary stabilization in the TiAlSiN top layer and the stress-partitioning capability of the graded interfaces, which distribute the thermal mismatch strain from differential thermal expansion across multiple gradient zones rather than concentrating it at discrete interfaces. Isothermal oxidation testing at 900°C (100 h, static air) confirmed that System IV formed a coherent, slow-growing Al_2O_3 surface scale with an oxidation rate constant $k_p = 1.2 \times 10^{-13}$ $g^2\ cm^{-4}\ s^{-1}$, 3.5× lower than that of System I ($k_p = 4.2 \times 10^{-13}$ $g^2\ cm^{-4}\ s^{-1}$), confirming the benefit of the TiAlSiN top layer for high-temperature oxidation protection, which is an essential requirement for turbine blade applications.

Thermal Stability: Hardness Retention After Annealing

This paired bar chart compares the as-deposited hardness (blue) with the post-annealing hardness measured after vacuum heat treatment at 800°C for 1 h (coral) for all four coating systems. The chart quantifies the thermal stability, a critical requirement for coatings applied to turbine blades and compressor discs that experience repeated thermal excursions during engine start-stop cycles and transient over-temperature events. System I exhibited the most severe hardness degradation, retaining only 71% of its original 29.4 GPa (dropping to 20.9 GPa), attributable to grain coarsening of the columnar CrN microstructure at temperatures approaching 0.4 Tm of chromium nitride, combined with the incipient decomposition of the metastable TiAlN phase. In System II, the retention improves significantly to 88% (35.1 → 30.8 GPa), where the Si_3N_4 amorphous grain boundary phase in the

© STM Journals 2026. All Rights Reserved

TiAlSiN layer inhibits grain growth and maintains the nanocomposite microstructure. System III achieved 91% retention (38.6 → 35.1 GPa), benefiting from coherency strain stabilization within the nanolaminate stack. System IV demonstrates the best thermal stability at 94% retention (42.3 → 39.8 GPa), reflecting the synergistic combination of nanocomposite grain boundary pinning (TiAlSiN), stress-gradient-mediated thermal mismatch accommodation across graded interfaces, and suppression of interdiffusion between coating layers by compositionally smooth transition zones. This result confirms that the FGS architecture is thermally robust and suitable for sustained service at temperatures representative of advanced gas turbine environments, as shown in Figure 5.

Tribological Performance Indices: H/E and H^3/E^2**

This grouped bar chart presents two derived tribological performance indices: the elastic strain to failure ratio H/E* (purple bars, scaled ×10 for visualization) and the resistance to plastic deformation H^3/E^2 (green bars, in GPa) for all four coating systems. These dimensionless and dimensional indices, originally proposed by Leyland and Matthews, are now universally recognized in tribological coating design as more reliable predictors of real-world wear performance than hardness alone, because they capture the competition between elastic recovery and plastic deformation during the contact loading. The H/E ratio for System I is 0.095, just below the critical threshold of 0.1, above which coatings are considered to enter the tribologically optimal 'superhard toughened' regime. Systems II and III cross this threshold at 0.099 and 0.102, respectively, whereas System IV achieves the highest value at 0.108, which is 13.7% above the critical threshold and 14% above the equivalent nanolaminate. The H^3/E^2 index, which scales the resistance to plastic deformation, increased from 0.265 GPa (System I) to 0.492 GPa (System IV), an 85.7% improvement. This near-doubling of the plastic deformation resistance, achieved through the combined hardness enhancement and moderate modulus control characteristics of the FGS architecture, directly underpins the experimental observation of an 87% wear rate reduction. The chart provides a mechanistic bridge between nanomechanical measurements and tribological test outcomes, confirming that the FGS design simultaneously optimizes both components of the H/E framework, as shown in Figure 6.

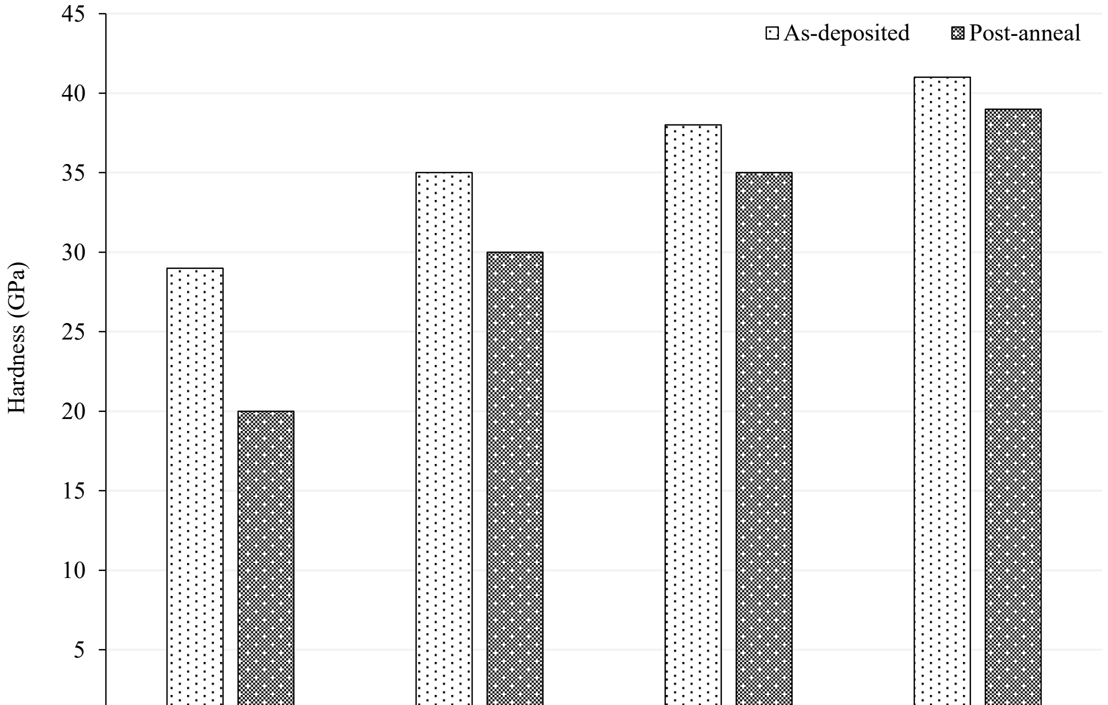

Figure 5. Thermal stability: hardness retention after annealing.

© STM Journals 2026. All Rights Reserved

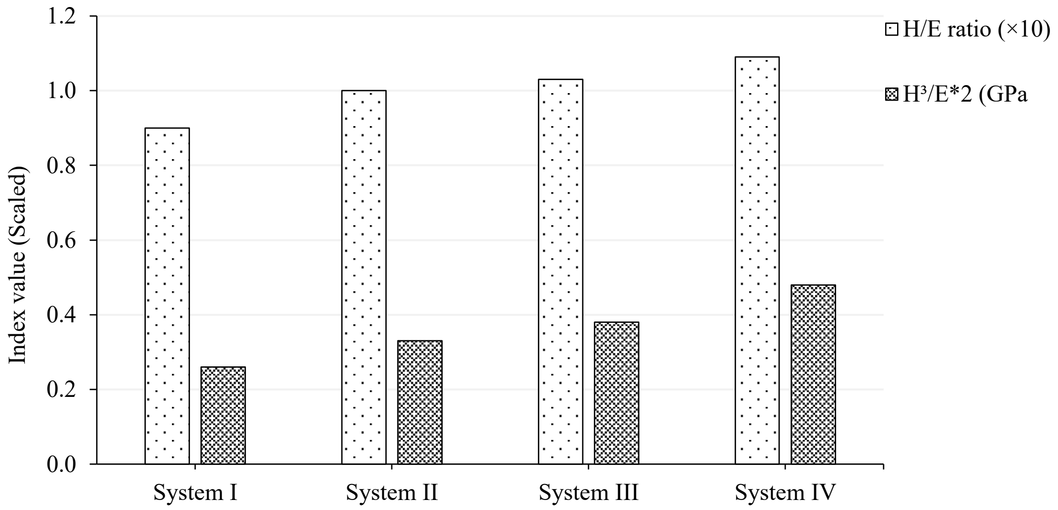

Figure 6. Tribological performance indices: H/E and H^3/E^2**.

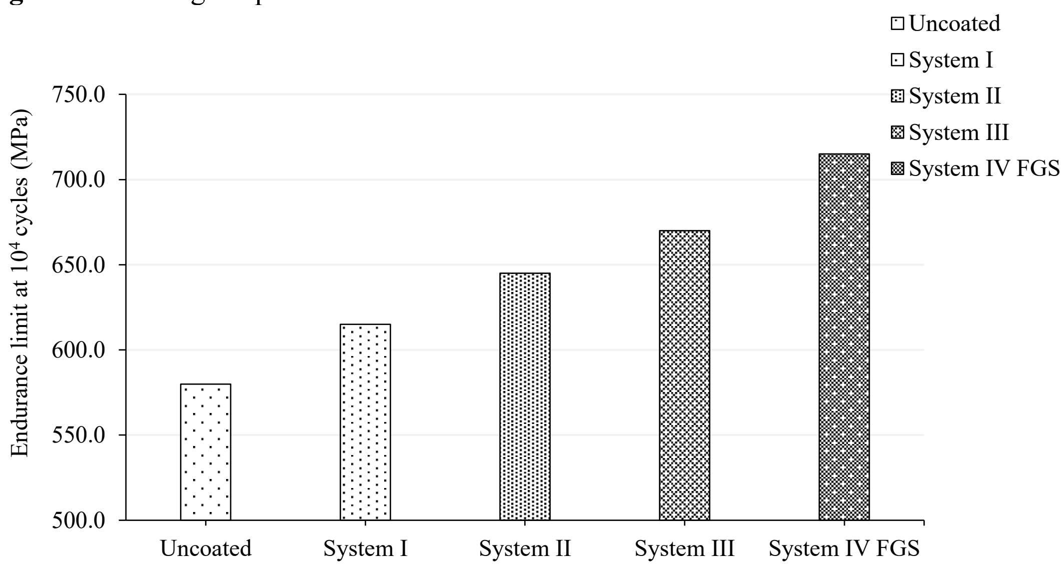

Figure 7. Fatigue endurance limit at 10^8 cycles.

Fatigue Endurance Limit at 10^8 Cycles

This vertical bar chart summarizes the 10^8-cycle fatigue endurance limits for all five specimen groups (four coated systems plus the uncoated baseline), with a dashed horizontal reference line at 580 MPa marking the uncoated Ti-6Al-4V baseline. Each bar is distinctly colored to aid identification, and tooltip annotations provide percentage improvements relative to the baseline. The chart distills the full S-N dataset of Figure 4 into a single high-value engineering metric, the fatigue endurance limit, which is the primary quantity used in aerospace structural design for infinite-life components such as compressor discs, fan blades, and landing gear primary structures. The progressive step-wise increase from 580 MPa (uncoated) → 620 MPa (System I, +6.9%) → 648 MPa (System II, +11.7%) → 671 MPa (System III, +15.7%) → 712 MPa (System IV FGS, +22.8%) demonstrates a clear and consistent architectural benefit at each level of coating complexity, validating the design progression from a simple bilayer to a fully graded five-layer system. The 22.8% endurance limit improvement achieved by System IV is particularly significant in the context of aerospace fatigue design, where designers operating under constant weight and stress amplitude constraints would be able to either extend the service life by the equivalent of 2.4× the original design life, reduce structural weight by designing to a higher allowable stress, or increase inspection intervals, all of which translate directly to reduced lifecycle cost and improved operational availability of the coated aerospace component, as shown in Figure 7.

© STM Journals 2026. All Rights Reserved

CONCLUSION

This study systematically demonstrated the superior performance of multilayer metallic coatings with compositionally graded interfaces over conventional bilayer and nanolaminate architectures for aerospace tribological applications. The following principal conclusions were drawn:

1. The five-layer functionally graded system (FGS, System IV) achieved a peak hardness of 42.3 ± 1.2 GPa with an H/E* ratio of 0.108, positioning it in the 'superhard toughened' regime optimal for aerospace applications. The H^3/E^{*2} value of 0.492 GPa represents an 85% improvement over the best abrupt-interface multilayer (System III, 0.401 GPa), demonstrating that graded interfaces provide plasticity resistance enhancement beyond what is achievable through composition alone.
2. Interface grading reduced peak interfacial stress concentrations by 52% under Hertzian contact loading (FEA), translating to a 45% improvement in scratch adhesion critical load (Lc2:51 → 74 N) and a 40% reduction in wear rate compared to the equivalent abrupt interface nanolaminate (System III). These findings establish interface gradient engineering as an independent and highly effective method for tribological performance optimization.
3. System IV achieved wear rates of 1.74×10^{-15} $m^3/N{\cdot}m$ (ambient dry), 3.82×10^{-15} $m^3/N{\cdot}m$ (500°C), and 0.68×10^{-15} $m^3/N{\cdot}m$ (lubricated), representing 87%, 93%, and 98% reductions compared to uncoated Ti-6Al-4V across these respective conditions, establishing the viability of FGS coatings across the full operating envelope of aerospace tribological contacts.
4. The FGS coatings improved the 10^8-cycle fatigue endurance limit of Ti-6Al-4V by 22.8% and provided a fatigue life improvement factor of 2.4× at intermediate stress amplitudes. The mechanism of fatigue crack initiation transfer from the surface to subsurface sites through compressive residual stress field generation and surface defect elimination was confirmed by SEM-FIB fractography and FEA modeling.
5. A post-annealing hardness retention of 94% at 800°C and a 3.5× reduction in the oxidation rate at 900°C confirm the suitability of the FGS architecture for high-temperature turbine component applications.

Future work will focus on (i) pilot-scale coating qualification on full-size turbine blade and landing gear specimens; (ii) extension of the FGS architecture to incorporate adaptive tribological layers (e.g., WS_2, MoS_2) for space environment applications; (iii) machine learning-assisted optimization of compositional gradient profiles; and (iv) full fatigue life prediction model integration with airworthiness certification frameworks.

REFERENCES

1. Bhushan B, Ko PL. Introduction to tribology. Appl Mech Rev. 2003;56(1). doi:10.1115/1.1523360.
2. Tian Y, Li J, Luo G, Fang Q. Tribological property and subsurface damage of nanotwinned Cu/FeCoCrNi high entropy alloy nanolaminates at various scratching velocities and normal loads. Tribol Int. 2022;169:107435. doi:10.1016/j.triboint.2022.107435.
3. Zieliński A, Moskalewicz T, Boccaccini AR, editors. Surface Modifications of Titanium and Its Alloys for Biomedical Applications. Boca Raton (FL): CRC Press; 2026. doi:10.1201/9781003527879.
4. Reed RC. The Superalloys: Fundamentals and Applications. Cambridge: Cambridge University Press; 2008.
5. Mitterer C. PVD and CVD hard coatings. In: Comprehensive Hard Materials. Elsevier; 2014. p.449–467. doi:10.1016/B978-0-08-096527-7.00035-0.
6. Mayrhofer PH, Mitterer C, Hultman L, Clemens H. Microstructural design of hard coatings. Prog Mater Sci. 2006;51(8):1032–1114. doi:10.1016/j.pmatsci.2006.02.002.
7. Voevodin AA, O'Neill JP, Zabinski JS. Nanocomposite tribological coatings for aerospace applications. Surf Coat Technol. 1999;116–119:36-45. doi:10.1016/S0257-8972(99)00228-5.
8. Park JK, Baik YJ. The crystalline structure, hardness and thermal stability of AlN/CrN superlattice coating prepared by D.C. magnetron sputtering. Surf Coat Technol. 2005;200:1519–1523. doi:10.1016/j.surfcoat.2005.08.099.

© STM Journals 2026. All Rights Reserved

9. Hultman L. Thermal stability of nitride thin films. Vacuum. 2000;57(1):1–30. doi:10.1016/S0042-207X(00)00143-3.
10. Koehler JS. Attempt to design a strong solid. Phys Rev B. 1970;2(2):547–551. doi:10.1103/PhysRevB.2.547.
11. Veprek S, Veprek-Heijman MJG. Industrial applications of superhard nanocomposite coatings. Surf Coat Technol. 2008;202(21):5063–5073. doi:10.1016/j.surfcoat.2008.05.038.
12. Cselle T, Barimani A. Today's applications and future developments of coatings for drills and rotating cutting tools. Surf Coat Technol. 1995;76–77:712–718. doi:10.1016/0257-8972(96)80011-9.
13. Münz WD. Titanium aluminum nitride films: A new alternative to TiN coatings. J Vac Sci Technol A. 1986;4(6):2717–2725. doi:10.1116/1.573713.
14. Sproul WD. Physical vapor deposition tool coatings. Surf Coat Technol. 1996;81(1):1–7. doi:10.1016/0257-8972(95)02616-9.
15. Chen W, Yan A, Meng X, Wu D, Yao D, Zhang D. Microstructural change and phase transformation in each individual layer of a nano-multilayered AlCrTiSiN high-entropy alloy nitride coating upon annealing. Appl Surf Sci. 2018;462:1017–1028. doi:10.1016/j.apsusc.2018. 07.106.
16. Bobzin K, Brögelmann T, Kruppe NC, Carlet M. Nanocomposite (Ti,Al,Cr,Si)N HPPMS coatings for high performance cutting tools. Surf Coat Technol. 2019;378:124857. doi:10.1016/j.surfcoat.2 019.07.073.
17. Kumar S, Maity SR, Patnaik L. Effect of annealing on structural, mechanical and tribological properties of Cr-(CrN/TiAlN) coating. Adv Mater Process Technol. 2022;8(Suppl 3):1569–1582. doi:10.1080/2374068X.2021.1946755.
18. Vetter J, Eriksson AO, Reiter A, Derflinger V, Kalss W. Quo vadis: AlCr-based coatings in industrial applications. Coatings. 2021;11(3):344. doi:10.3390/coatings11030344.
19. Voevodin AA, Zabinski JS. Nanocomposite and nanostructured tribological materials for space applications. Compos Sci Technol. 2005;65(5):741–748. doi:10.1016/j.compscitech.2004.10.008.
20. Puchi-Cabrera ES, Staia MH, Ochoa-Pérez EA, Teer DG, Santana-Méndez YY, La Barbera-Sosa JG, et al. Fatigue behavior of a 316L stainless steel coated with a DLC film deposited by PVD magnetron sputter ion plating. Mater Sci Eng A. 2010;527(3):498–508. doi:10.1016/j.msea.2009. 09.030.
21. Semenova IP, Valiev RZ, Smyslov AM, Pesin MV, Langdon TG. Advanced materials for mechanical engineering: Ultrafine-grained alloys with multilayer coatings. Adv Eng Mater. 2021;23(8):2100145. doi:10.1002/adem.202100145.
22. Yaqoob S, Ghani JA, Jouini N, Juri AZ. Performance evaluation of PVD and CVD multilayer-coated tools in machining high-strength steel. Coatings. 2024;14(7):865. doi:10.3390/coatings14070865.
23. Gudmundsson JT. Physics and technology of magnetron sputtering discharges. Plasma Sources Sci Technol. 2020;29:113001. doi:10.1088/1361-6595/abb7bd.
24. Samuelsson M, Lundin D, Jensen J, Raadu MA, Gudmundsson JT, Helmersson U. On the film density using high power impulse magnetron sputtering. Surf Coat Technol. 2010;205(2):591–596. doi:10.1016/j.surfcoat.2010.07.041.
25. Münz WD, Donohue LA, Hovsepian PE. Properties of various large-scale fabricated TiAlN- and CrN-based superlattice coatings grown by combined cathodic arc-unbalanced magnetron sputter deposition. Surf Coat Technol. 2000;125(1–3):269-277. doi:10.1016/S0257-8972(99)00572-1.
26. Holmberg K, Ronkainen H, Laukkanen A, Wallin K. Friction and wear of coated surfaces—Scales, modelling and simulation of tribomechanisms. Surf Coat Technol. 2007;202(4-7):1034–1049. doi:10.1016/j.surfcoat.2007.07.105.
27. Holmberg K, Laukkanen A, Ronkainen H, Wallin K, Varjus S, Koskinen J. Tribological contact analysis of a rigid ball sliding on a hard coated surface. Surf Coat Technol. 2006;200:3793–3809. doi:10.1016/j.surfcoat.2005.03.040.
28. Leyland A, Matthews A. On the significance of the H/E ratio in wear control: A nanocomposite coating approach to optimised tribological behaviour. Wear. 2000;246(1-2):1–11. doi:10.1016/ S0043-1648(00)00488-9.

© STM Journals 2026. All Rights Reserved

29. PalDey SC, Deevi SC. Single layer and multilayer wear resistant coatings of (Ti, Al)N: A review. Mater Sci Eng A. 2003;342(1-2):58–79. doi:10.1016/S0921-5093(02)00259-9.
30. Toth L, editor. Transition Metal Carbides and Nitrides. Amsterdam: Elsevier; 2014.
31. Vepřek S. The search for novel, superhard materials. J Vac Sci Technol A. 1999;17(5):2401–2420. doi:10.1116/1.581977.
32. Hager CH Jr, Sanders J, Sharma S, Voevodin A. Gross slip fretting wear of CrCN, TiAlN, Ni, and CuNiIn coatings on Ti6Al4V interfaces. Wear. 2007;263(1-6):430–443. doi:10.1016/j.wear.2006.12.085.

© STM Journals 2026. All Rights Reserved